Supplementary Information (SI) for Physical Chemistry Chemical Physics.
This journal is © the Owner Societies 2026

Slide Electrification Charge Can Exist without Residual Liquid Film: KPFM Measurements near Receding Three-Phase Contact Lines

Yuki Ishihara,[a] Hideaki Teshima,[*a,b] Qin–Yi Li,[a,b] and Koji Takahashi,[a,b]

a. Department of Aeronautics and Astronautics, Kyushu University, 744 Motooka, Nishi–Ku, Fukuoka 819–0395, Japan. E-mail: hteshima05@aero.kyushu-u.ac.jp

b. International Institute for Carbon–Neutral Energy Research (WPI–I2CNER), Kyushu University, 744 Motooka, Nishi–Ku, Fukuoka 819–0395, Japan.

Supplementary Information

Table of content

Supplementary Note 1: Conversion from surface potential to surface charge density.

Using the parallel–plate capacitor approximation for the probe–substrate gap in KPFM, the surface charge density σ_{KPFM} on an insulating thin–film substrate is given as follows [1,2]:

$$\sigma_{\mathrm{KPFM}} \approx \frac{V_{\mathrm{S}} - V_{\mathrm{ref}}}{d_{\mathrm{film}}} {\varepsilon_{\mathrm{r}}}^{\mathrm{film}} \varepsilon_0 \tag{S1}$$

Here, V_{S} is the measured surface potential, V_{ref} is the contact potential difference with the base substrate, d_{film} is the dielectric–film thickness (in the experiment, we used 300 nm thermally grown SiO_2 (Fig. S1)), ${\varepsilon_{\mathrm{r}}}^{\mathrm{film}}$ is the relative permittivity of the dielectric film, and ε_0 is the vacuum permittivity. For example, using typical values for a SiO_2 film—$V_{\mathrm{S}} = -3.0\ \mathrm{V}$, $V_{\mathrm{ref}} = -0.5\ \mathrm{V}$, $d_{\mathrm{film}} = 300\ \mathrm{nm}$, ${\varepsilon_{\mathrm{r}}}^{\mathrm{film}} = 3.9$, and $\varepsilon_0 = 8.854 \times 10^{-12}\ \mathrm{F \cdot m^{-1}}$—the calculated σ_{KPFM} is approximately $-288\ \mu\mathrm{C \cdot m^{-2}}$.

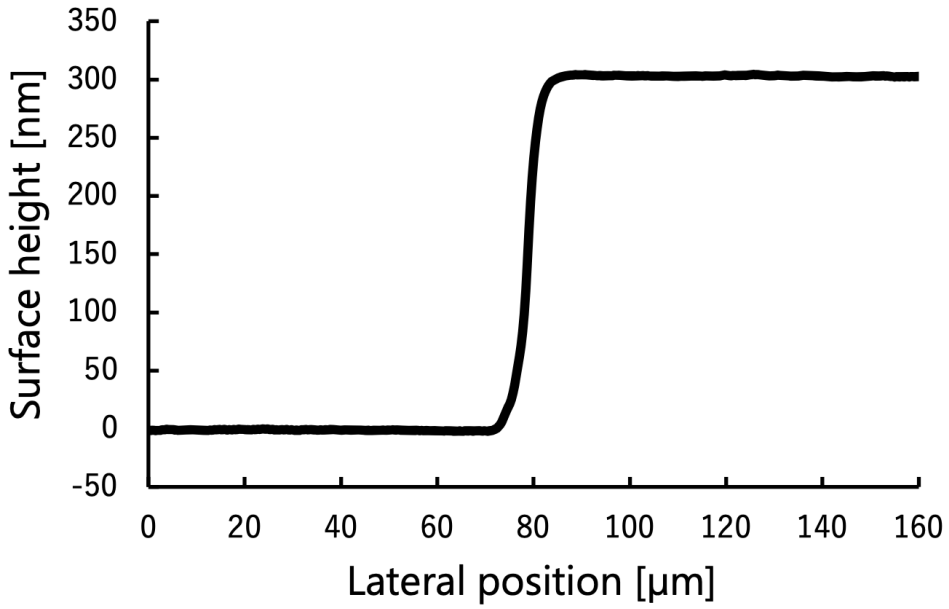

Fig. S1. Surface-height profile measured by a stylus profilometer across the boundary between the Si substrate exposed by selective BHF etching and the remaining SiO_2-coated region. Because buffered HF selectively removes SiO_2, a clean Si/SiO_2 step was obtained. The measured step height is approximately 300 nm, confirming the SiO_2 film thickness used for d_{film} in Eq. (S1).

In the present KPFM measurements, the conductive Si substrate was used as the electrical reference. Experimentally, the backside of the Si substrate was electrically connected to the sample stage using conductive tape or an equivalent method, and the stage was connected to the AFM instrument ground. Thus, the potential of the conductive Si substrate served as the ground reference throughout the measurements. Because the surface potential and the converted charge density are linearly related through Eq. (S1), only the axis units differ, while the spatial pattern and profile shape remain unchanged (Fig. S2).

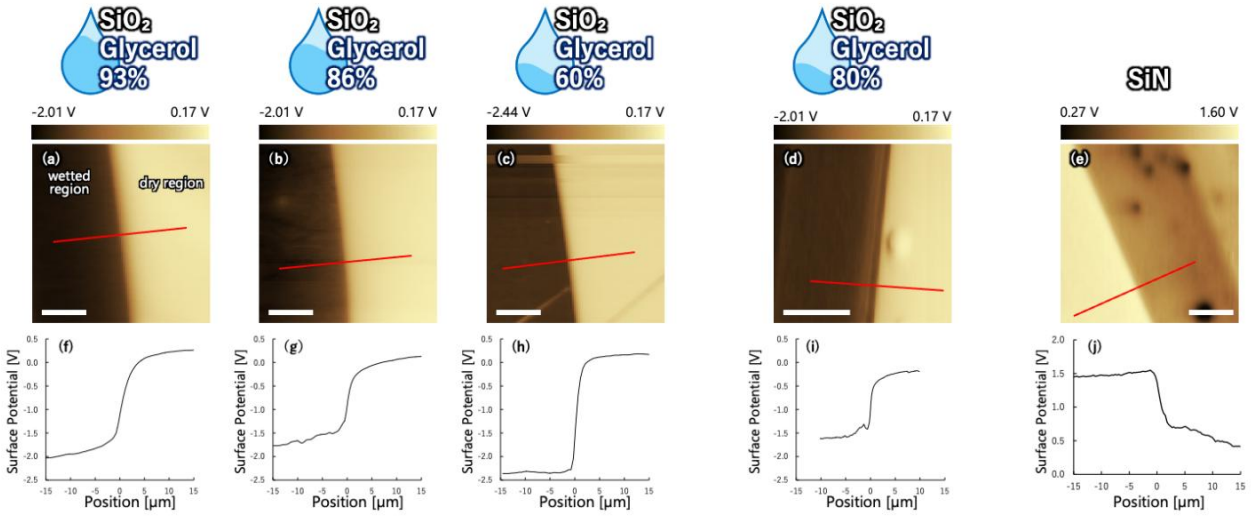

Fig. S2. Original KPFM CPD (surface-potential) data corresponding to the datasets analyzed in the manuscript and SI. (a–e) Unconverted CPD maps for SiO2 surfaces measured with glycerol/water droplets of 93 wt%, 86 wt%, 60 wt%, and 80 wt%, and for the SiN case, respectively. The red lines indicate the positions used for profile extraction. (f–j) Corresponding surface-potential profiles extracted along the lines shown in panels (a–e), respectively. Because the conversion from CPD to surface charge density is linear [Eq. (S1)], the spatial patterns and profile shapes are unchanged, and only the units differ from those in the converted charge-density plots. The 80 wt% SiO_2 dataset is included here as discussed in the SI. Each scale bar is 10 µm.

Supplementary Note 2: Experimental result with 80 wt% glycerol (Fig. S3)

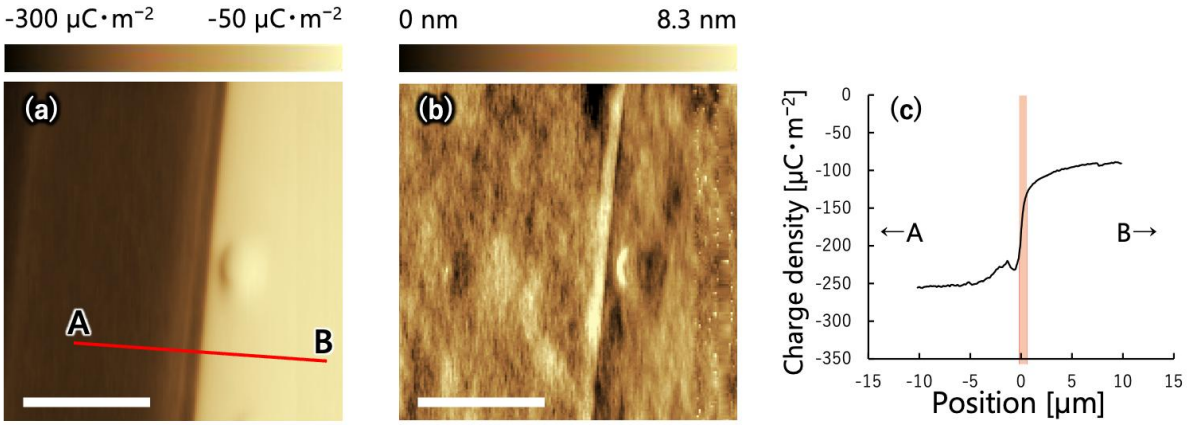

Fig. S3. KPFM experimental results for an 80 wt% glycerol–water solution droplet on a SiO_2 substrate. The calculated bulk Debye length is, $\lambda_{\mathrm{bulk}} \approx 750\ \mathrm{nm}$. (a) Surface charge–density map. (b) Corresponding topography acquired over the same area as in (a). Each scale bar is 10 μm. (c) Line profile along the red A–B line in (a); Position = 0 is defined as the location where the surface charge–density gradient is maximal. To quantify the steepness of the charge–density transition, we defined the 25–75% transition width, W_{25-75}, as the distance over which the surface charge density changes from 25% to 75% of its total variation across the analyzed window (−10 to +10 μm). We obtained $W_{25-75} = 0.74\ \mu\mathrm{m}$.

Supplementary Note 3: KPFM measurement becomes unstable when attempting to measure a well-wetted surface

When we attempted to measure a substrate rendered hydrophilic by atmospheric plasma bearing a 1–2 μm-thick liquid film (as seen in coherence scanning interferometry (CSI) inspection), the KPFM tip–sample feedback became unstable, producing distorted images, as shown in Fig. S4.

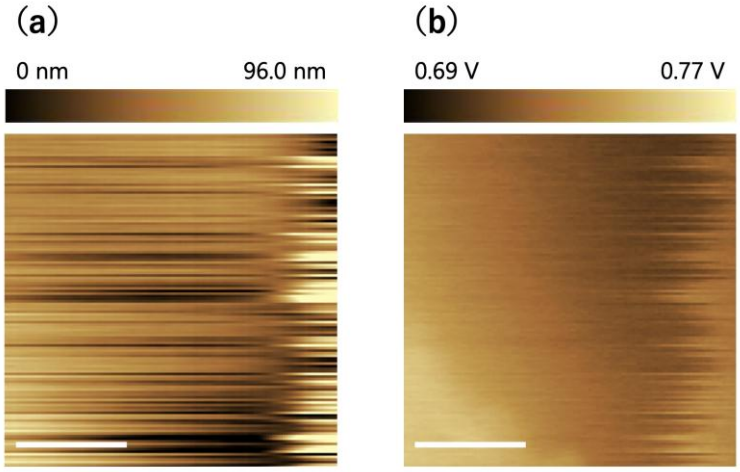

Fig. S4. KPFM images acquired on a well-wetted surface. (a) Topography image; pronounced line-by-line distortions are evident. (b) Surface-potential image over the same area as in (a); although the overall potential trend is discernible, the data exhibit substantial noise and the probe–surface non-contact condition cannot be reliably maintained. Therefore, these measurements should be regarded as qualitative rather than quantitative. Each scale bar is 20 μm.

This result indirectly indicates that KPFM measurements cannot be performed stably on insufficiently dried substrate surfaces. In contrast, in the experimental setup used in the main text, no such noise or scan distortions were observed. Based on these observations, we conclude that no residual-liquid-film-like structures remained in the measured area. Note that this result does not rule out the presence of water molecules on the substrate surface itself.

We conducted complementary AFM measurements on a SiO_2 sample both before droplet deposition and after TPCL recession. AFM topographic images obtained in tapping mode (Fig. S5a) and contact mode (Fig. S5b) revealed the presence of small dot-like objects before droplet deposition. Although it is known that in contact mode, soft objects are compressed and become invisible in the height image, the objects were still visible on the contact mode image, indicating that these are solid contamination, such as nanoparticles. AFM topographic measurements were again performed after TPCL recession. As a result, the tapping-mode image (Fig. S5c) and contact-mode image (Fig. S5d) showed almost the same topography, and revealed no nanodroplets or liquid film. From these results, the possibility that a thin residual liquid film partially covers the substrate can be excluded.

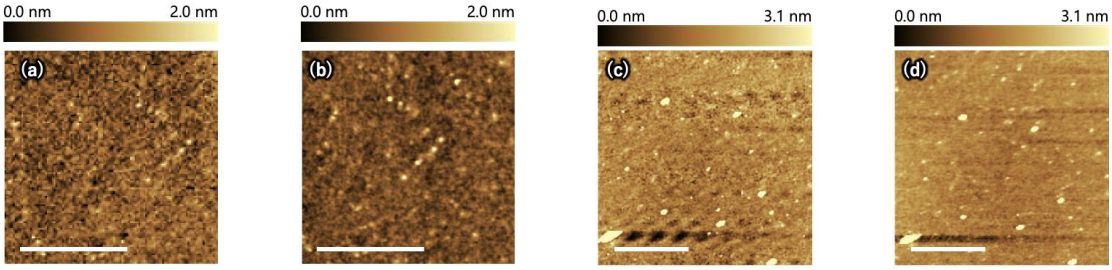

Fig. S5. AFM characterization of the SiO_2 surface before droplet deposition and after TPCL recession. (a) AFM tapping-mode and (b) AFM contact-mode topography before droplet deposition, and (c) tapping-mode and (d) contact-mode images after the TPCL recession. (a, b) and (c, d) are not taken at the same location. Each scale bar is 1 μm.

On the other hand, there remains the possibility that the entire AFM measurement area is covered by a sub-nanometer liquid film that follows the surface morphology of the Si substrate. In such a case, its presence cannot be distinguished in the AFM topographic image. However, if such a continuous water layer existed on the surface, rather than retaining charge, more rapid charge relaxation would be expected because of large charge diffusion coefficients, as reported in Ref. 18. Also, based on these considerations, we infer that charge stabilization can occur even without a continuous water film.

Supplementary Note 4: Ion concentration and pH

The ionic speciation in glycerol–water solutions is considered. In a glycerol–water mixture, the ionic species that may be present include those arising from the autoprotolysis of water, the weak-acid dissociation of dissolved carbonic acid species, and the (effective) monoprotic weak-acid dissociation of glycerol treated as a triol. Prior to presenting the detailed numerical procedure, it is convenient to formulate an ion-balance relation based on electroneutrality. Here, $[\chi]$denotes the concentration of ionic species χ. For convenience, unless explicitly stated otherwise, we do not distinguish between $[\mathrm{H^+}]$ and $[\mathrm{H_3O^+}]$ in what follows. The overall charge balance can be summarized conceptually as follows:

$$[\mathrm{H^+}] = [\mathrm{OH^-}] + [\mathrm{HCO_3^-}] + 2\left[\mathrm{CO_3^{2-}}\right] + [\mathrm{C_3H_7O_3^-}]. \tag{S2}$$

Accordingly, the ionic composition of a glycerol–water solution can be obtained by numerically solving the coupled dissociation equilibria together with the charge-balance condition. The computational steps are outlined below. First, the conversion from composition (wt%) to volumes and volume fractions is introduced

$$V_{\mathrm{gly}} = \frac{m_{\mathrm{gly}}}{\rho_{\mathrm{gly}}}, \qquad V_{\mathrm{w}} = \frac{m_{\mathrm{w}}}{\rho_{\mathrm{w}}}, \qquad V_{\mathrm{tot}} = V_{\mathrm{gly}} + V_{\mathrm{w}}, \qquad \varphi_{\mathrm{gly}} = \frac{V_{\mathrm{gly}}}{V_{\mathrm{tot}}}, \qquad \varphi_{\mathrm{w}} = \frac{V_{\mathrm{w}}}{V_{\mathrm{tot}}} = 1 - \varphi_{\mathrm{gly}}. \tag{S3}$$

Here, V_{gly}, V_{w}, and V_{tot} denote the volumes of glycerol, water, and the mixture, respectively. The quantities m_{gly} and m_{w} are the masses of glycerol and water, respectively, and ρ_{gly} and ρ_{w} are their densities. At 25 °C, typical values are $\rho_{\mathrm{gly}} \approx 1.26 \times 10^3\ \mathrm{kg \cdot m^{-3}}$ and $\rho_{\mathrm{w}} \approx 9.97 \times 10^2\ \mathrm{kg \cdot m^{-3}}$. The symbols φ_{gly} and φ_{w} represent the corresponding volume fractions.[3]

Next, the water activity is evaluated. The water activity denoted by a_{w} is obtained by linear interpolation of the tabulated values as a function of φ_{gly}. As numerical examples, the water activity was approximately 0.68 at $\varphi_{\mathrm{gly}} = 60\ \%$ and approximately 0.42 at $\varphi_{\mathrm{gly}} = 80\%$.[4]

$$a_{\mathrm{w}} \equiv a_{\mathrm{w}}(\varphi_{\mathrm{gly}}) \tag{S4}$$

For notational simplicity, when a quantity is formally a function $f(x)$, the explicit dependence on the variable may be omitted and the quantity written simply as f. The autoprotolysis of water is conceptually represented by

$$2\mathrm{H_2O} \rightleftharpoons \mathrm{H_3O^+} + \mathrm{OH^-}, \tag{S5}$$

and the equilibrium constant K_{w} is represented as $K_{\mathrm{w,ref}} \approx [\mathrm{H^+}][\mathrm{OH^-}]$. At 25 °C, a typical value is $K_{\mathrm{w,ref}} \approx 1.0 \times 10^{-14}$ (in concentration units, i.e., $(\mathrm{mol \cdot L^{-1}})^2$). Because the extent of water autoprotolysis is suppressed as the water activity decreases, the following relation is adopted:

$$K_{\mathrm{w,act}} = {a_{\mathrm{w}}}^2 K_{\mathrm{w,ref}}. \tag{S6}$$

Here, $K_{\mathrm{w,ref}}$ is the equilibrium constant for water autoprotolysis without activity correction, and $K_{\mathrm{w,act}}$denotes the activity-corrected value. Related dissociation reactions and equilibrium constants for water, the carbonic system, and glycerol are written as follows.

$$[\mathrm{CO_2}^*] \equiv [\mathrm{CO_2(aq)}] + [\mathrm{H_2CO_3}] \approx [\mathrm{CO_2(aq)}] \tag{S7}$$

$$\mathrm{CO_2}^* + \mathrm{H_2O} \rightleftharpoons \mathrm{H^+} + \mathrm{HCO_3}^-, \qquad \mathrm{HCO_3}^- \rightleftharpoons \mathrm{H^+} + \mathrm{CO_3}^{2-} \tag{S8}$$

$$K_{1,\mathrm{ref}} \approx \frac{[\mathrm{H^+}][\mathrm{HCO_3}^-]}{[\mathrm{CO_2}^*]}, \qquad K_{2,\mathrm{ref}} \approx \frac{[\mathrm{H^+}][\mathrm{CO_3}^{2-}]}{[\mathrm{HCO_3}^-]} = \frac{[\mathrm{H^+}]^2[\mathrm{CO_3}^{2-}]}{K_{1,\mathrm{ref}}[\mathrm{CO_2}^*]} \tag{S9}$$

$$\mathrm{C_3H_8O_3} \rightleftharpoons \mathrm{H^+} + \mathrm{C_3H_7O_3}^- \tag{S10}$$

$$K_{\mathrm{a,gly,ref}} \approx \frac{[\mathrm{H^+}][\mathrm{C_3H_7O_3}^-]}{[\mathrm{C_3H_8O_3}]} \tag{S11}$$

At 25 °C, typical values are $K_{1,\mathrm{ref}} \approx 4.45 \times 10^{-7}$, $K_{2,\mathrm{ref}} \approx 4.69 \times 10^{-11}$, and $K_{\mathrm{a,gly,ref}} \approx 7.1 \times 10^{-15}$ (in concentration units, i.e., $\mathrm{mol \cdot L^{-1}}$).[3,5,6] Equilibrium constants may vary slightly with the dielectric permittivity of the solvent and with water activity. Therefore, the relative permittivity of the mixed solvent is first evaluated. The relative permittivity is approximated by linear mixing with volume fraction.

$$\varepsilon_{\mathrm{mix}} = \varphi_{\mathrm{w}}\varepsilon_{\mathrm{w}} + \varphi_{\mathrm{gly}}\varepsilon_{\mathrm{gly}} \tag{S12}$$

Here, $\varepsilon_{\mathrm{mix}}$, ε_{w}, and $\varepsilon_{\mathrm{gly}}$ denote the relative permittivities of the mixture, water, and glycerol, respectively. At 25 °C, typical values are $\varepsilon_{\mathrm{w}} \approx 78.3$ for water and $\varepsilon_{\mathrm{gly}} \approx 42.5$ for glycerol.[7] Next, a dielectric-induced shift of dissociation equilibria is introduced via a $\mathrm{p}K \equiv -\log_{10} K$ shift model:

$$\Delta\left(\frac{1}{\varepsilon}\right) \equiv \frac{1}{\varepsilon_{\mathrm{mix}}} - \frac{1}{\varepsilon_{\mathrm{w}}} \tag{S13}$$

and

$$\mathrm{p}K_{\mathrm{eff}} = \mathrm{p}K_{\mathrm{ref}} + \beta\Delta\left(\frac{1}{\varepsilon}\right). \tag{S14}$$

Here, the symbol K denotes an equilibrium constant for the dissociation reaction of interest. The parameter β is an empirical coefficient, and $\beta = 1.4 \times 10^2$ is adopted in this study.[5,6] This approach is applied to the activity-corrected water autoprotolysis constant and to the first dissociation constant of the carbonic system and the glycerol dissociation constant, i.e., to $K_{\mathrm{w,act}}$, $K_{1,\mathrm{ref}}$, and $K_{\mathrm{a,gly,ref}}$, in order to obtain the equilibrium constants ultimately used in calculations, $K_{\mathrm{w,eff}}$, $K_{1,\mathrm{eff}}$, and $K_{\mathrm{a,gly,eff}}$. For water, $K_{\mathrm{w,act}}$is used here in place of $K_{\mathrm{w,ref}}$. The second dissociation of the carbonic system is expected to contribute negligibly under the present conditions; therefore, the dielectric-permittivity-induced $\mathrm{p}K$shift is not applied to K_2, and we simply set $K_{2,\mathrm{eff}} \approx K_{2,\mathrm{ref}}$.

The dissolved carbonic species in the solution are then considered. A reference concentration in pure water is first computed using Henry's law: $[\mathrm{CO_2}^*]_{\mathrm{ref}} = k_{\mathrm{H}} p_{\mathrm{CO_2}}$ where k_{H} is Henry's constant and $p_{\mathrm{CO_2}}$ is the partial pressure of carbon dioxide in air. In this study, typical values of $k_{\mathrm{H}} \approx 3.4 \times 10^{-2}\ \mathrm{mol \cdot L^{-1} \cdot atm^{-1}}$ and $p_{\mathrm{CO_2}} \approx 4.0 \times 10^{-4}\ \mathrm{atm}$ are used.[8] In the mixed solvent, the equilibrium concentration is approximated using the water volume fraction:

$$[\mathrm{CO_2}^*]_{\mathrm{mix,eq}} = \varphi_{\mathrm{w}} [\mathrm{CO_2}^*]_{\mathrm{ref}}. \tag{S15}$$

The viscosity of the mixed solvent is approximated by a logarithmic (geometric-mean) mixing rule:

$$\eta_{\mathrm{mix}} = \eta_{\mathrm{w}} \left(\frac{\eta_{\mathrm{gly}}}{\eta_{\mathrm{w}}} \right)^{\kappa} \tag{S16}$$
$$\left(\Leftrightarrow \ln \eta_{\mathrm{mix}} = (1-\kappa) \ln \eta_{\mathrm{w}} + \kappa \ln \eta_{\mathrm{gly}} \right).$$

Here, η_{mix}, η_{w}, and η_{gly} denote the viscosities of the mixture, water, and glycerol, respectively. In this study, representative values of $\eta_{\mathrm{w}} \approx 1.0\ \mathrm{mPa \cdot s}$ and $\eta_{\mathrm{gly}} \approx 945\ \mathrm{mPa \cdot s}$ are adopted as reference viscosities. The parameter κ is defined by $\kappa \equiv \frac{\mathrm{wt\%}}{100}$ i.e., a dimensionless quantity based on the glycerol mass percentage. The diffusion coefficient of $\mathrm{CO_2}$ in the mixture is estimated using the Stokes–Einstein relation:

$$D_{\mathrm{CO_2,mix}} = \frac{k_{\mathrm{B}} T}{6\pi \eta_{\mathrm{mix}} r_{\mathrm{CO_2}}} \tag{S17}$$

where $r_{\mathrm{CO_2}}$ is the effective hydrodynamic radius of $\mathrm{CO_2}$, $\approx 0.13\ \mathrm{nm}$, k_{B} is the Boltzmann constant, $\approx 1.38 \times 10^{-23}\ \mathrm{J \cdot K^{-1}}$, and T is the absolute temperature.[9] The volumetric mass-transfer coefficient is then assumed to depend on composition through a power-law dependence on diffusivity:

$$k_{\mathrm{L}} a_{\mathrm{mix}} = k_{\mathrm{L}} a_{\mathrm{ref}} \left(\frac{D_{\mathrm{CO_2,mix}}}{D_{\mathrm{CO_2,ref}}} \right)^{0.5} \tag{S18}$$

where $D_{\mathrm{CO_2,ref}}$ is the diffusion coefficient of $\mathrm{CO_2}$ in water, $k_{\mathrm{L}} a_{\mathrm{mix}}$ is the volumetric mass-transfer coefficient in the mixed solvent, and $k_{\mathrm{L}} a_{\mathrm{ref}}$ is its value in pure water. In this study, $k_{\mathrm{L}} a_{\mathrm{ref}} = 5.0 \times 10^{-4}\ \mathrm{s^{-1}}$ is adopted as a representative reference value. Here, $D_{\mathrm{CO_2,ref}}$ is evaluated using the same Stokes–Einstein relation with the viscosity of pure water.[9]

The time evolution of dissolved $\mathrm{CO_2}$ is then described. When $\mathrm{CO_2}$ dissolves from the gas phase (air) into the liquid phase (glycerol–water solution), a flux into the liquid is driven by the difference between the interfacial equilibrium concentration $[\mathrm{CO_2}^*]_{\mathrm{mix,eq}}$ (set by Henry's law) and the bulk concentration $[\mathrm{CO_2}^*]_{\mathrm{mix,aq}}(t)$. This is approximated as

$$\frac{\mathrm{d}[{CO_2}^*]_{\mathrm{mix,aq}}}{\mathrm{d}t} = k_{\mathrm{L}} a_{\mathrm{mix}} \left([{CO_2}^*]_{\mathrm{mix,eq}} - [{CO_2}^*]_{\mathrm{mix,aq}}(t) \right). \tag{S19}$$

Accordingly,

$$[{CO_2}^*]_{\mathrm{mix,aq}}(t) = [{CO_2}^*]_{\mathrm{mix,eq}} + \left([{CO_2}^*]_{\mathrm{mix,aq}}(0) - [{CO_2}^*]_{\mathrm{mix,eq}} \right) \exp(-k_{\mathrm{L}} a_{\mathrm{mix}} t). \tag{S20}$$

Based on these assumptions, we consider the charge balance of the solution. Chemical equilibria at each time t are then expressed as follows. For water autoprotolysis,

$$[\mathrm{OH^-}](t) = \frac{K_{\mathrm{w,eff}}}{[\mathrm{H^+}](t)}. \tag{S21}$$

For the carbonic system,

$$[{HCO_3}^-](t) = K_{1,\mathrm{eff}} \frac{[{CO_2}^*]_{\mathrm{mix,aq}}(t)}{[\mathrm{H^+}](t)}, \qquad [{CO_3}^{2-}](t) = K_{1,\mathrm{eff}} K_{2,\mathrm{eff}} \frac{[{CO_2}^*]_{\mathrm{mix,aq}}(t)}{\{[\mathrm{H^+}](t)\}^2}. \tag{S22}$$

For glycerol, the dissociation contribution is assumed to scale with the water volume fraction φ_{w}, and the effective anion concentration is written as

$$[{C_3H_7O_3}^-]_{\mathrm{eff}}(t) = \varphi_{\mathrm{w}} K_{\mathrm{a,gly,eff}} \frac{[\mathrm{Glycerol_{tot}}](t)}{K_{\mathrm{a,gly,eff}} + [\mathrm{H^+}](t)}. \tag{S23}$$

Here, $[\mathrm{Glycerol_{tot}}] = [\mathrm{C_3H_8O_3}] + [{C_3H_7O_3}^-]$ is the total (analytical) glycerol concentration including both dissociated and undissociated forms. The quantity $[{C_3H_7O_3}^-]_{\mathrm{eff}}(t)$ is used in both the charge-balance relation and the ionic-strength calculation. With these relations, the electroneutrality condition is solved numerically by applying Newton's method to the following function G:

$$G([\mathrm{H^+}]) = [\mathrm{H^+}] - [\mathrm{OH^-}](t) - [{HCO_3}^-] - 2[{CO_3}^{2-}] - [{C_3H_7O_3}^-]_{\mathrm{eff}} = 0 \tag{S24}$$

$$\left(\Leftrightarrow [\mathrm{H^+}] - \frac{K_{\mathrm{w,eff}}}{[\mathrm{H^+}]} - K_{1,\mathrm{eff}} \frac{[{CO_2}^*]_{\mathrm{mix,aq}}}{[\mathrm{H^+}]} - 2K_{1,\mathrm{eff}} K_{2,\mathrm{eff}} \frac{[{CO_2}^*]_{\mathrm{mix,aq}}}{[\mathrm{H^+}]^2} - \varphi_{\mathrm{w}} K_{\mathrm{a,gly,eff}} \frac{[\mathrm{Glycerol_{tot}}]}{K_{\mathrm{a,gly,eff}} + [\mathrm{H^+}]} = 0 \right).$$

The Newton update is given by $[\mathrm{H^+}]_{\mathrm{k+1}} = [\mathrm{H^+}]_{\mathrm{k}} - G / \frac{\mathrm{d}G}{\mathrm{d}[\mathrm{H^+}]}$. Based on this calculation, the pH of the glycerol–water solution is approximately 6.0–6.5.

Supplementary Note 5: Charge carriers

The SiO_2 surface reacts with ambient moisture to form abundant silanol groups (SiOH), a fraction of which dissociates as:[10]

$$\mathrm{SiOH} + \mathrm{H_2O} \rightleftharpoons \mathrm{SiO^-} + \mathrm{H_3O^+}. \quad (S25)$$

Likewise, SiN presents amino-terminated sites (≡Si–NH_2) that undergo acid–base dissociation upon exposure to moisture.[11]

$$\mathrm{SiNH_2} + \mathrm{H_2O} \rightleftharpoons \mathrm{SiNH_3^+} + \mathrm{OH^-} \quad (S26)$$

The point of zero charge (PZC) of SiO_2 is about pH ≈ 3,[10] so contact with a weakly acidic glycerol solution (containing dissolved CO2) places the surface under conditions pH > PZC; consequently, $\mathrm{SiO^-}$ becomes the dominant charge carrier and negative charging prevails. In contrast, SiN surfaces possess amino groups (–NH_2) and have a higher PZC near pH ≈ 6.5; under contact with a weakly acidic glycerol solution, $-NH_3^+$ can become the dominant carrier, so the surface can become positively charged depending on the conditions.

Supplementary Note 6: Ion strength and the Debye length of the solution

The ionic strength I is defined by

$$I \equiv \frac{1}{2}\sum_i c_i {z_i}^2 \tag{S27}$$

where c_i is the molar concentration of ionic species i and z_i is its charge number. For the present system, the sum includes $\mathrm{H^+}$, $\mathrm{OH^-}$, $\mathrm{{HCO_3}^-}$, $\mathrm{{CO_3}^{2-}}$, and $\mathrm{C_3H_7O_3^-}$ as applicable. The Debye length $\lambda(\varphi_{\mathrm{gly}})$ is:

$$\lambda(\varphi_{\mathrm{gly}}) = \sqrt{\frac{\varepsilon_{\mathrm{mix}}(\varphi_{\mathrm{gly}})\varepsilon_0 k_{\mathrm{B}} T}{2N_{\mathrm{A}} e^2 I}} \tag{S28}$$

where $\varepsilon_{\mathrm{mix}}(\varphi_{\mathrm{gly}})$ is the relative permittivity of the mixed solvent, T is the absolute temperature, N_{A} is Avogadro's constant, and e is the elementary charge. The ionic strength I is evaluated in SI units $(\mathrm{mol{\cdot}m^{-3}})$ using c_i in $\mathrm{mol{\cdot}m^{-3}}$, so that contributions from multivalent ions (e.g., $\mathrm{{CO_3}^{2-}}$) are naturally accounted for through the ${z_i}^2$ weighting. When concentrations are obtained in $\mathrm{mol{\cdot}L^{-1}}$, they are converted to SI units via $c_i(\mathrm{mol{\cdot}m^{-3}}) = 10^3\, c_i(\mathrm{mol{\cdot}L^{-1}})$.

Supplementary Note 7: Diffusion coefficient of glycerol aqueous solutions

Using Vignes' equation to estimate the diffusion coefficient of a binary liquid mixture, we approximate the diffusion coefficient of the glycerol–water solution as:[12]

$$\ln D_{\mathrm{ion,eff}}(z) = (1-z)\ln D_{\mathrm{ion,water}} + z \ln D_{\mathrm{ion,glycerol}} \quad (\mathrm{S29})$$
$$\left(\Leftrightarrow D_{\mathrm{ion,eff}}(z) = {D_{\mathrm{ion,water}}}^{1-z} {D_{\mathrm{ion,glycerol}}}^{z}\right)$$

where z is the mole fraction of glycerol in the solution, $D_{\mathrm{ion,eff}}(z)$ is the diffusion coefficient of the solution, $D_{\mathrm{ion,water}} = 1.0 \times 10^{-9}\ \mathrm{m^2 \cdot s^{-1}}$, and $D_{\mathrm{ion,glycerol}} = 1.0 \times 10^{-11}\ \mathrm{m^2 \cdot s^{-1}}$.[9] Furthermore, considering that the volumetric molar concentration of glycerol is $13.7\ \mathrm{mol \cdot L^{-1}}$ and that of water is $55.5\ \mathrm{mol \cdot L^{-1}}$, the mole fraction of glycerol is expressed as:

$$z = \frac{13.7\varphi_{\mathrm{gly}}}{55.5 - 41.8\varphi_{\mathrm{gly}}} \quad (\mathrm{S30})$$

For $0.50 \leq \varphi_{\mathrm{gly}} \leq 0.95$, $D_{\mathrm{ion,eff}}$ is on the order of $10^{-10}\ \mathrm{m^2 \cdot s^{-1}}$. Considering that pipetting induces internal droplet velocities on the order of $10^{-5}\ \mathrm{m \cdot s^{-1}}$, the stretching of the Debye length by flow proceeds much faster than self–diffusion of ions, and TPCL recession can efficiently strip ions from the solid–liquid interface. For simplicity, we use the calculated Debye length at $t = 10$ min. However, the key point is that a consistent trend is observed: even as t increases, the Debye length increases with increasing glycerol fraction.

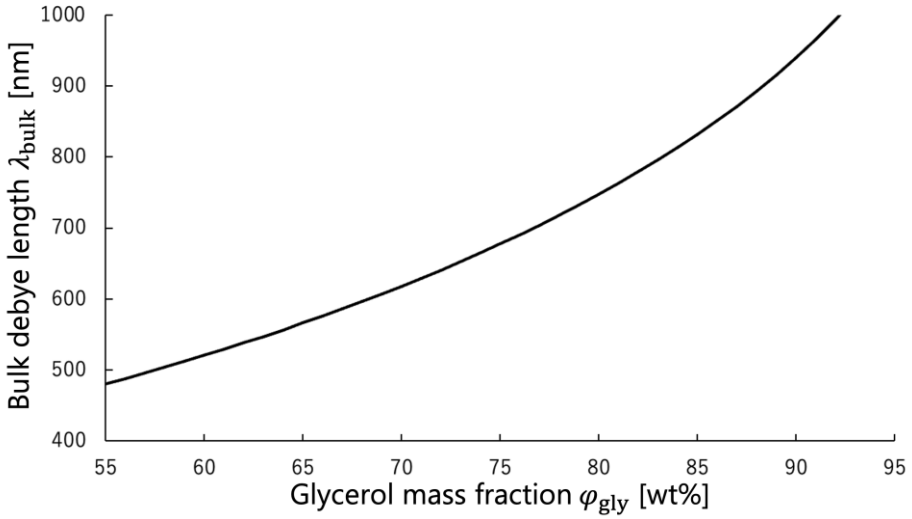

Fig. S6. Calculated bulk Debye length, λ_{bulk}, as a function of glycerol mass fraction (wt%) in glycerol–water mixtures. The monotonic increase reflects the reduction in ionic strength with increasing glycerol content under the present assumptions.

Supplementary Note 8: Wedge-induced EDL distortion

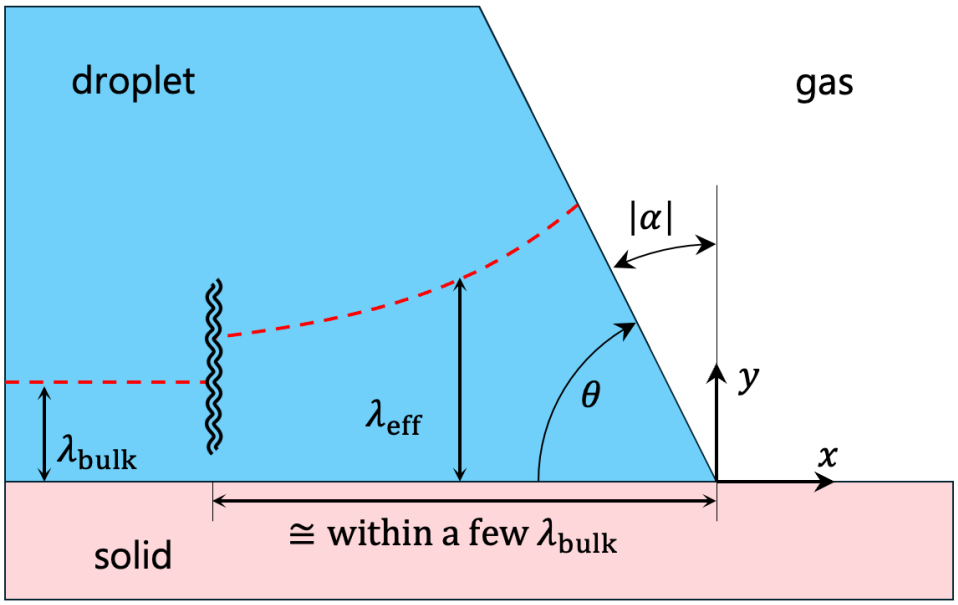

Fig. S7. Schematic of the wedge-induced EDL–distortion model near the three-phase contact line (TPCL). The finite contact angle θ increases the effective EDL thickness from λ_{bulk} (far from the TPCL) to λ_{eff} in the wedge region. Here, λ_{eff} is only a conceptual expression; in the model, it should be interpreted as λ_{CA} or λ_{Pe}, depending on the conditions. This geometric distortion modifies the interfacial charge density associated with solid–liquid contact.[13,14,15]

For a wedge-shaped liquid domain with contact angle θ, applying Gauss's law yields an expression for the isopotential surfaces. Using λ_{bulk} as the characteristic isopotential-surface spacing, the effective local Debye length near the contact line, denoted by λ_{CA}, is given as follows:[13]

$$\lambda_{\mathrm{CA}}(x) = f(X)\lambda_{\mathrm{bulk}},\ (x \le 0) \tag{S31}$$

with,

$$f(X) = 1 - \left(1 - \frac{1-d}{c}\cos\alpha\right) \times \exp\left(-\tan\alpha \frac{-X + (1-d)\sin\alpha}{c - (1-d)\cos\alpha}\right)$$

$$c = 1 + 0.36\alpha, \qquad d = \ln\frac{\pi + 2\alpha}{\pi}, \qquad \alpha = \theta - \frac{\pi}{2}, \qquad X = \frac{x}{\lambda_{\mathrm{bulk}}}.$$

Here, x value is defined in an absolute coordinate and X is a coordinate normalized by λ_{bulk}, with the contact line at the origin; the droplet occupies the region $x \le 0$ (Fig. S7). Using $f(X)$ from Eq. (S31), the solid–liquid interfacial charge density, denoted by $\sigma_{\mathrm{SL}}(x)$, accounting for the wedge-induced EDL distortion, is given as follows:

$$\sigma_{\mathrm{SL}}(x) = \sigma_{\mathrm{SL},0}\frac{\lambda_{\mathrm{bulk}}}{\lambda_{\mathrm{CA}}(x)} = \frac{\sigma_{\mathrm{SL},0}}{f(X)} \tag{S32}$$

Here, $\sigma_{\mathrm{SL},0}$ is the solid–liquid interfacial charge density far from the contact line. Noting that $f(X)$ is normalized by the λ_{bulk}, Eqs. (S31) and (S32) imply that the solid–liquid interfacial charge is strongly affected within a distance of a few Debye lengths from the contact line. They further indicate that a longer Debye length leads to a shallower gradient of σ_{SL} near the contact line.

First, we fitted the measurements using only the wedge-induced EDL distortion effect. We defined the far-field solid–liquid interfacial charge density, denoted by $\sigma_{\mathrm{SL},0}$, as the measured value farthest from the boundary on the wetted region in the charge-density maps (Fig. 1(a–c) and Fig. S3). Also, we defined the pre-contact solid–gas interfacial charge density, denoted by $\sigma_{\mathrm{SG},0}$, as the measured value farthest from the boundary on the dry region side in the same maps. We then defined the effective charging amount, denoted by $\Delta\sigma$, as follows:

$$\Delta\sigma = \sigma_{\mathrm{SL},0} - \sigma_{\mathrm{SG},0} \tag{S33}$$

In the model accounting only for the wedge-induced EDL distortion effect, the fitted surface charge density, denoted by $\sigma_{\mathrm{CA}}(x)$, using Eqs. $(\mathrm{S32}-\mathrm{S34})$, is given as follows:

$$\sigma_{\mathrm{CA}}(x) = \begin{cases} \dfrac{\Delta\sigma}{f(X)} + \sigma_{\mathrm{SG},0}, & (x \le 0) \\ \sigma_{\mathrm{SG},0}, & (x > 0) \end{cases}. \tag{S34}$$

For the contact angle, we used the measured value on SiO_2, $\theta = 66°$ which was the same for all four samples. λ_{bulk} for all cases were estimated from the solution composition and were 1020 nm, 850 nm, 520 nm, and 750 nm for Fig. 1(a), (b), (c), and Fig. S3 respectively. The model calculation corresponds to the green dotted curve in Fig. 4 and Fig. S9. The calculation suggests that a lower glycerol fraction—i.e., a shorter Debye length—leads to a steeper surface charge gradient in the wetted region, consistent with the experimental result. This is because a longer Debye length suppresses solid–liquid contact charging farther from the contact line, whereas a shorter Debye length confines this suppression to only the immediate vicinity of the contact line.

Supplementary Note 9: Estimation of flow velocity

For a spherical-cap droplet, the volume V is conveniently written as a function of the contact-line radius R and contact angle θ.

$$V = \frac{\pi R^3}{3}\Psi(\theta), \qquad \Psi(\theta) = \frac{(1-\cos\theta)^2(2+\cos\theta)}{\sin^3\theta} \tag{S35}$$

Given a pipetting withdrawal rate $V' = \mathrm{d}V/\mathrm{d}t$, and assuming that the contact angle remains approximately constant during recession, the contact-line speed is written as

$$U_{\mathrm{CL}} = \frac{V'}{\pi R^2 \Psi(\theta)}. \tag{S36}$$

When approximately one-half of a 3 μL droplet is withdrawn over ~5 seconds, local mass conservation near the contact line suggests that both the horizontal and the normal (vertical) velocities in the vicinity of the three-phase contact line (TPCL) are of the order of U_{CL}, which is estimated to be on the order of $10^{-5}\ \mathrm{m\cdot s^{-1}}$. In the present study, a representative value of U_{CL} is $40\times10^{-6}\ \mathrm{m\cdot s^{-1}}$.

Near the contact line, the free-surface geometry can be approximated by a wedge. Denoting the local film thickness by h, one obtains

$$h(s) \approx s\tan\theta \tag{S37}$$

where s is the distance from the contact line defined by $s \equiv |x| \quad (s \geq 0)$. Based on this approximation, local mass conservation in the near-contact-line region implies that the local volumetric flux around the circumference is approximately conserved, leading to $\tilde{u}(s)h(s) \approx \text{constant}$. Since $h(s) \propto s$, this relation suggests an inverse-proportional scaling of the near-contact-line velocity, $\tilde{u}(s) \propto \frac{1}{s}$. To avoid the divergence at $s = 0$, a cutoff length ℓ_{cutoff} is introduced, and the following regularized form is assumed: $\tilde{u}(s) \propto \frac{\ell_{\mathrm{cutoff}}}{s+\ell_{\mathrm{cutoff}}}$. In addition, due to geometric symmetry, the horizontal velocity is expected to vanish near the droplet center. Incorporating this constraint, the horizontal velocity distribution $u(s)$ along the solid–liquid interface is modeled as follows:

$$u(s) = \begin{cases} U_{\mathrm{CL}}\dfrac{U(s)-U(L)}{1-U(L)}, & (0 \leq s \leq L) \\ 0, & (s > L) \end{cases} \tag{S38}$$

with

$$U(s) \equiv \left(\frac{\ell_{\mathrm{cutoff}}}{s+\ell_{\mathrm{cutoff}}}\right). \tag{S39}$$

This construction yields a continuous velocity profile that satisfies the following limiting behaviors: the characteristic velocity scale at the contact line is set by U_{CL}, the near-contact-line decay follows approximately $U_{\mathrm{CL}}\left(\frac{\ell_{\mathrm{cutoff}}}{s+\ell_{\mathrm{cutoff}}}\right)$, and the velocity approaches zero toward the droplet center.

Supplementary Note 10: Flow effect

Interfacial flow induced by recession tends to pull the EDL away from the interface; accordingly, the effective local Debye length accounting for this effect, denoted by λ_{Pe}, is given as follows: [16,17]

$$\lambda_{\mathrm{Pe}}(x) = \lambda_{\mathrm{CA}}(x)\frac{Pe(x) + \sqrt{Pe(x)^2 + 4}}{2} \tag{S40}$$

with

$$Pe(x) = \frac{u(|x|)\lambda_{\mathrm{CA}}(x)}{D_{\mathrm{ion,eff}}}. \tag{S41}$$

Here, Pe is the Péclet number, defined with $u(|x|)$ as the flow velocity, λ_{CA} as the characteristic length, and $D_{\mathrm{ion,eff}}$ as the ionic diffusion coefficient of the liquid phase. Under these conditions, the solid–liquid interfacial charge density $\sigma_{\mathrm{SL}}(x)$, combined with the flow effect, is given as follows:

$$\sigma_{\mathrm{SL}}(x) = \frac{\sigma_{\mathrm{SL},0}}{f(X)}\frac{2}{Pe(x) + \sqrt{Pe(x)^2 + 4}}. \tag{S42}$$

Near the TPCL, the faster the velocity and the slower the ionic diffusion—i.e., the larger the Pe—the more strongly the interfacial charge changes. In the model additionally accounting for the flow effect, the fitted surface charge density, denoted by $\sigma_{\mathrm{Pe}}(x)$, using Eqs. (S34) and (S42), is given as follows:

$$\sigma_{\mathrm{Pe}}(x) = \begin{cases} \dfrac{\Delta\sigma}{f(X)}\dfrac{2}{Pe(x) + \sqrt{Pe(x)^2 + 4}} + \sigma_{\mathrm{SG},0}, & (x \le 0) \\ \sigma_{\mathrm{SG},0}, & (x > 0) \end{cases}. \tag{S43}$$

The model calculation corresponds to the light-blue dashed curve in Fig. 4 and Fig. S9. The calculation suggests that the fit in the wetted region improves relative to the model without the flow effect. However, there is a step at $x = 0$. To account for the experimental results, we therefore introduce the charge relaxation term on the solid–gas surface.

Supplementary Note 11: Charge relaxation

In this study, acquisition of a single KPFM image required approximately 15 min. Because a KPFM image is obtained by scanning, the acquisition time differs for each line; thus, a single image inherently contains up to ~15 min of time offset (i.e., sub-hour time-resolved information). We therefore compared the potential/charge profiles following the acquisition order within a single image, but did not observe a clear decrease in potential or any pronounced charge relaxation during the measurement (Figs. S8a, S8c, and S8d). Accordingly, we consider that the charge distributions discussed in this study can be treated as quasi-static, at least over the duration required to acquire a single image (~15 min).

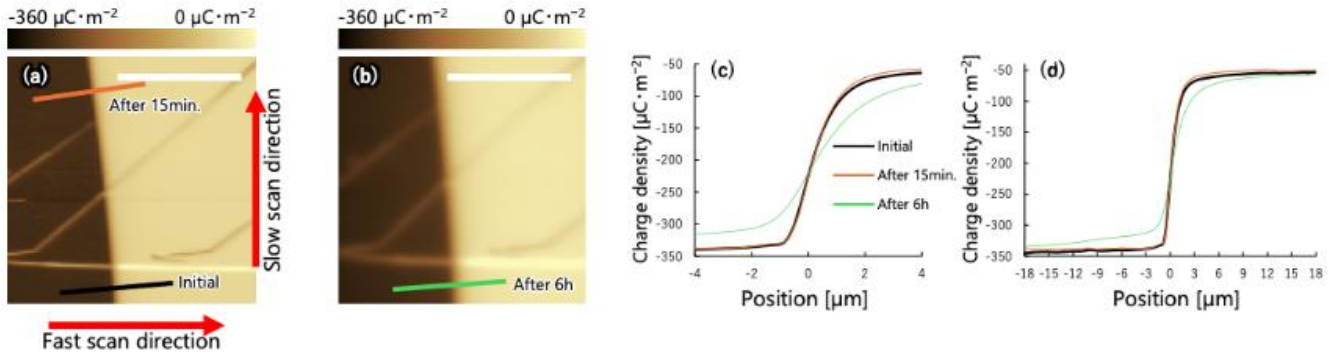

Fig. S8. Time-dependent comparison of KPFM measurements acquired at nearly the same area after TPCL recession. (a) Surface charge-density map acquired within 5 min after completion of the TPCL-recession procedure. The slow- and fast-scan directions are indicated by the red arrows. (b) Surface charge-density map acquired at nearly the same location after approximately 6 h. (c,d) Line profiles near the boundary. The black, orange, and green curves in panels (c) and (d) correspond to the lines of the same colors shown in panels (a) and (b). Panel (c) shows a magnified view of the boundary region, whereas panel (d) shows a wider view. The profiles indicate that no pronounced relaxation is evident within the acquisition time of a single image, whereas smoothing of the boundary profile is observed after several hours. Position = 0 is defined as the point at which the surface-charge-density gradient is maximal. Each scale bar is 25 μm.

To examine whether surface charge relaxation occurs on a longer time scale, we remeasured nearly the same area approximately 6 hours later. As a result, we confirmed that the overall charge distribution was largely preserved, while relaxation (smoothing) progressed, particularly in the vicinity of the boundary (Figs. S8b, S8c, and S8d).

Accordingly, we introduce a relaxation hypothesis whereby charge relaxation, which typical for solid-gas interface[18], occurs at the boundary between the dry region and the wetted region, leading to a continuous surface-charge distribution. We consider that charge relaxation is primarily governed by (i) drift of charges driven by the in-plane electric field arising from the surface potential gradient and (ii) charge diffusion. Assuming that the mobile carriers at the surface are predominantly protons, as a simplest approximation, the drift and diffusion contributions can be expressed, respectively, as follows:

$$\frac{\partial \sigma}{\partial t} \approx \mu\sigma \frac{\partial E}{\partial x}, \qquad \frac{\partial \sigma}{\partial t} \approx D \frac{\partial^2 \sigma}{\partial x^2}$$

Here, σ is the surface charge density, E is the in-plane electric field, μ is the mobility of carriers, and D is the diffusion coefficient of carriers. According to these expressions, the relative importance of drift and diffusion can be approximately evaluated as $\frac{\mu EL}{D}$ using a characteristic length scale L. Immediately after TPCL recession, because the initial surface potential gradient is considered to be substantially large at the boundary, the drift-driven relaxation can proceed rapidly, which result in the relaxed charge curves (initial curves in Figs. S8c and S8d). In contrast, the characteristic time for diffusion is approximately given by $\tau \approx L^2/D$.[19, 20]

During the measurement, we assume that the temporal variation of $\sigma(x)$ is negligibly small. Hence, the experimentally observed profile is interpreted as a frozen state after charge has already redistributed, and the charge-transfer process itself is not directly captured. To represent the post-relaxation distribution, we introduce a correction term $\delta\sigma(x)$ that is localized in the vicinity of $x = 0$.

$$\sigma_{\mathrm{rel}}(x) = \begin{cases} \dfrac{\Delta\sigma}{f(X)} \dfrac{2}{Pe(x) + \sqrt{Pe(x)^2 + 4}} + \sigma_{SG,0} + \delta\sigma(x), & (x \le 0) \\ \sigma_{\mathrm{SG,0}} + \delta\sigma(x), & (x > 0) \end{cases} \tag{S44}$$

Assuming local charge conservation around $x = 0$, the correction term satisfies

$$\int_{-\infty}^{0} \delta\sigma(x)\mathrm{d}x = -Q_{\mathrm{tr}}, \qquad \int_{0}^{+\infty} \delta\sigma(x)\mathrm{d}x = +Q_{\mathrm{tr}}. \tag{S45}$$

Here, Q_{tr} denotes the total amount of charge transferred across the boundary (per unit depth in the out-of-plane direction). In addition to fulfilling these conservation constraints, we prescribe $\delta\sigma(x)$ as a combination of an exponential form and an exponential multiplied by a first-order polynomial, anticipating a future extension in which the slope at $x = 0$ is enforced to match across the boundary. This yields

$$\delta\sigma(x) = \begin{cases} -\dfrac{Q_{\mathrm{tr}}}{\ell_{\mathrm{sm}}} \exp\left(\dfrac{x}{\ell_{\mathrm{sm}}}\right) - \dfrac{\sigma_{\mathrm{Pe}}{}'(0^-)}{2} (x + \ell_{\mathrm{sm}}) \exp\left(\dfrac{x}{\ell_{\mathrm{sm}}}\right), & (x \le 0) \\ +\dfrac{Q_{\mathrm{tr}}}{\ell_{\mathrm{sm}}} \exp\left(\dfrac{-x}{\ell_{\mathrm{sm}}}\right), & (x > 0) \end{cases} \tag{S46}$$

In this formulation, ℓ_{sm} serves as a fitting parameter that characterizes the strength (or spatial extent) of relaxation. We represent one-sided limits at the origin using $0^-$and 0^+. For example, the left-hand limit of the

derivative of $\sigma_{\mathrm{Pe}}(x)$ is written as $\sigma_{\mathrm{Pe}}{}'(0^-) \equiv \lim_{x\to -0} \frac{\mathrm{d}\sigma_{\mathrm{Pe}}(x)}{\mathrm{d}x}$. Imposing continuity of $\sigma_{\mathrm{rel}}(x)$ at $x = 0$ leads to the following relation for Q_{tr}:

$$\sigma_{\mathrm{Pe}}(0^-) - \frac{Q_{\mathrm{tr}}}{\ell_{\mathrm{sm}}} - \frac{\sigma_{\mathrm{Pe}}{}'(0^-)}{2}\ell_{\mathrm{sm}} = \sigma_{\mathrm{SG},0} + \frac{Q_{\mathrm{tr}}}{\ell_{\mathrm{sm}}} \tag{S47}$$

$$\left(\Leftrightarrow Q_{\mathrm{tr}} = \frac{1}{2}\left(\sigma_{\mathrm{Pe}}(0^-) - \sigma_{\mathrm{SG},0}\right)\ell_{\mathrm{sm}} - \frac{\sigma_{\mathrm{Pe}}{}'(0^-)}{4}{\ell_{\mathrm{sm}}}^2\right).$$

Accordingly, the relaxed surface-charge distribution is given by

$$\sigma_{\mathrm{rel}}(x) = \begin{cases} \dfrac{\Delta\sigma}{f(X)}\dfrac{2}{Pe(x) + \sqrt{Pe(x)^2 + 4}} + \sigma_{\mathrm{SG},0} - \left(\dfrac{Q_{\mathrm{tr}}}{\ell_{\mathrm{sm}}} + \dfrac{\sigma_{\mathrm{Pe}}{}'(0^-)}{2}(x + \ell_{\mathrm{sm}})\right)\exp\left(\dfrac{x}{\ell_{\mathrm{sm}}}\right), & (x \le 0) \\ \sigma_{\mathrm{SG},0} + \dfrac{Q_{\mathrm{tr}}}{\ell_{\mathrm{sm}}}\exp\left(\dfrac{-x}{\ell_{\mathrm{sm}}}\right), & (x > 0) \end{cases}. \tag{S48}$$

If slope matching at $x = 0$ is additionally imposed, one obtains $\sigma_{\mathrm{rel}}{}'(0^-) = \sigma_{\mathrm{rel}}{}'(0^+) \Leftrightarrow \sigma_{\mathrm{Pe}}{}'(0^-) + \delta\sigma'(0^-) = \delta\sigma'(0^+)$. In particular, the continuous boundary value at $x = 0$ becomes $\sigma_{\mathrm{rel}}(0) = \frac{1}{2}\left(\sigma_{\mathrm{Pe}}(0^-) + \sigma_{SG,0}\right) - \frac{\sigma_{Pe}{}'(0^-)}{4}\ell_{sm}$.

At the same time, the exponential relaxation term used here is not intended to identify a single specific mechanism. Rather, it is introduced as a convenient effective representation to capture the profile smoothing observed near the boundary.

Supplementary Note 12: Calculation results with 80 wt% glycerol (Fig. S9)

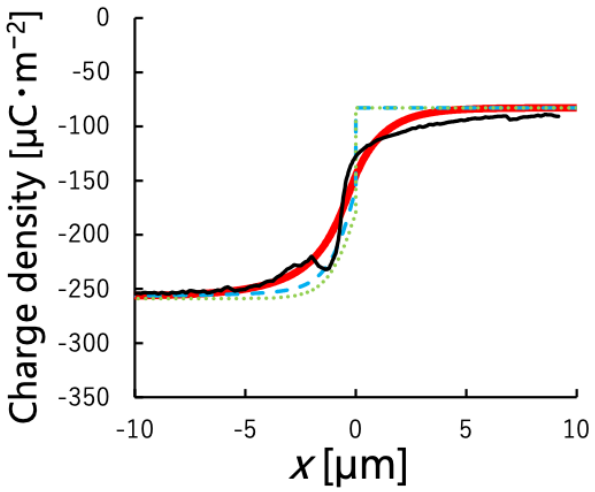

Fig. S9. Calculation results for an 80 wt% glycerol–water solution. The black curve shows the measured surface charge–density profile, plotted after applying a constant horizontal shift to the experimental x-coordinate (equivalent to the previously used "position"), $\Delta x = -0.659\ \mu\mathrm{m}$, $x_{\mathrm{exp}} \rightarrow x_{\mathrm{exp}} + \Delta x$, to minimize the root mean squared error (RMSE) over $-10 \leq x \leq 10\ \mu\mathrm{m}$; the model x-coordinate is left unchanged. The green dotted curve represents the model including only wedge-induced EDL distortion, the light-blue dashed curve represents the model including both wedge-induced distortion and the flow effect, and the red curve represents the full model including wedge-induced distortion, the flow effect, and charge relaxation. Model curves were computed using $\lambda_{\mathrm{bulk}} = 750\ \mathrm{nm}$, $\ell_{\mathrm{sm}} = 1.297\ \mu\mathrm{m}$ and $D_{\mathrm{ion,eff}} = 1.01 \times 10^{-10}\ \mathrm{m^2 \cdot s^{-1}}$.

References

1. S. Lin, L. Xu, A. C. Wang and Z. L. Wang, Nature Communications, 2020, 11, 399, DOI: 10.1038/s41467-019-14278-9.
2. J. F. Gonzalez, A. M. Somoza and E. Palacios-Lidon, Physical Chemistry Chemical Physics, 2017, 19, 27299–27304, DOI: 10.1039/c7cp05401g.
3. OECD SIDS Programme, OECD SIDS, 2002, SIDS Initial Assessment Report for SIAM 14 (Glycerol).
4. H. Nakagawa and T. Oyama, Frontiers in Chemistry, 2019, 7, 731, DOI: 10.3389/fchem.2019.00731.
5. G. Fonrodona, C. Rafols, E. Bosch and M. Roses, Analytica Chimica Acta, 1996, 335, 291–302, DOI: 10.1016/S0003-2670(96)00329-7.
6. L. Falciola, A. Fierro, P. R. Mussini, T. Mussini, M. Rossi and D. Dumitrel, Journal of Chemical & Engineering Data, 2009, 54, 286–293, DOI: 10.1021/je800310a.
7. A. A. Maryott and E. R. Smith, National Bureau of Standards Circular, 1951, 514, Table of Dielectric Constants of Pure Liquids.
8. R. Sander, Atmospheric Chemistry and Physics, 2023, 23, 10901–12440, DOI: 10.5194/acp-23-10901-2023.
9. J. B. Segur and H. E. Oberstar, Industrial & Engineering Chemistry, 1951, 43(9), 2117–2120.
10. M. Kosmulski, Journal of Colloid and Interface Science, 2004, 275, 214–224, DOI: 10.1016/j.jcis.2004.02.029.
11. L. S. Cerovic, S. K. Milonjic, D. Bahloul-Hourlier and B. Doucey, Colloids and Surfaces A: Physicochemical and Engineering Aspects, 2002, 197, 147–156, DOI: 10.1016/S0927-7757(01)00863-9.
12. A. Vignes, Industrial & Engineering Chemistry Fundamentals, 1966, 5(2), 189–199.
13. A. Dorr and S. Hardt, Physical Review E, 2012, 86, 022601, DOI: 10.1103/PhysRevE.86.022601.
14. S. Das and S. K. Mitra, Physical Review E, 2013, 88, 033021, DOI: 10.1103/PhysRevE.88.033021.
15. M. Mussotter and M. Bier, Physical Review E, 2017, 96, 032605, DOI: 10.1103/PhysRevE.96.032605.
16. A. D. Ratschow, H.-J. Butt, S. Hardt and S. A. L. Weber, Soft Matter, 2025, 21, 1251–1262, DOI: 10.1039/d4sm01289e.
17. A. D. Ratschow, L. S. Bauer, P. Bista, S. A. L. Weber, H.-J. Butt and S. Hardt, Physical Review Letters, 2024, 132, 224002, DOI: 10.1103/PhysRevLett.132.224002.
18. X. Bai, A. Riet, S. Xu, D. J. Lacks and H. Wang, The Journal of Physical Chemistry C, 2021, 125, 11677–11686, DOI: 10.1021/acs.jpcc.1c02272.
19. T. M. Squires and S. R. Quake, Reviews of Modern Physics, 2005, 77, 977–1026, DOI: 10.1103/RevModPhys.77.977.
20. C. Yang, X. Xing, Z. Li and S. Zhang, Polymers, 2020, 12, 138, DOI: 10.3390/polym12010138.